Atmospheric Research 326 (2025) 108313

Contents lists available at ScienceDirect

Atmospheric Research

journal homepage: www.elsevier.com/locate/atmosres

Uncertainty of "Pangu-Weather" in Bay of Bengal storm track forecasts: Target observation perspective

Zeyun Zhou [a], Wansuo Duan [b,*], Ruowen Yang [a,*], Xiaohao Qin [b,c], Yonghui Li [b]

[a] Department of Atmospheric Science, Yunnan University, Kunming 650500, China

[b] Key Laboratory of Earth System Numerical Modeling and Application, Institute of Atmospheric Physics, Chinese Academy of Sciences, Beijing 100029, China

[c] Laboratory of Numerical Modeling for Atmospheric Sciences and Geophysical Fluid Dynamics, Institute of Atmospheric Physics, Chinese Academy of Sciences, Beijing 100029, China

ARTICLE INFO

Keywords:
Target observation
Bay of Bengal storms
Pangu-Weather model
Conditional nonlinear optimal perturbation

ABSTRACT

The Bay of Bengal storms (BoB storms) are the most catastrophic weather conditions in the region of Bay of Bengal and pose a significant threat to countries within and adjacent to the region, highlighting the urgent need for accurate forecasts to increase disaster prevention and mitigation efforts. However, sparse observations limit the accuracy of the BoB storm forecasts. Current numerical forecast systems adopt "target observation" strategy to increase additional observations and improve the forecast skill, but still face challenge of low efficiency and allow more model error effects on efficacy of additional observations. The study adopts a highly efficient Artificial Intelligence-driven "Pangu-Weather" model and constructs an optimization system for identifying sensitive areas of target observations associated with the BoB storm track forecasts based on the conditional nonlinear optimal perturbation (CNOP) method. The CNOP method comprehensively accounts for nonlinear processes and has been verified to be superior to traditional linear approximation methods, such as singular vector, adjoint sensitivity, and ETKF. Based upon this system, the sensitive areas for target observations were determined for 12 forecasts of four strong BoB storms and their roles were evaluated in terms of the improvement of the storm track forecast level through observing system simulation experiments. The results demonstrate that preferentially improving the accuracy of the initial conditions in the sensitive areas, compared with doing it in randomly selected areas, can be more significant to upgrade the storm track forecast level; however, such upgrades only hold for the forecast duration of 24 h. This result provides hints for the potential of the Pangu-Weather model in forecasting BoB storms and has the implication that the predictability of the "Pangu-Weather" model with respect to the BoB storm tracks is dominantly constrained by model error effects after 24 h. It suggests that the improvement of model architecture is necessary for prolonging the predictability time of Pangu-Weather with respect to the BoB storms.

1. Introduction

Tropical cyclones (TCs) occurring over the Bay of Bengal (BoB) are commonly referred to as "BoB storms". The annual frequency of BoB storm occurrences is relatively lower, approximately 6.8 per year (Liang et al., 2020), and their intensities are also generally weak; however, these storms often cause more severe damages than the TCs of similar scales over the western North Pacific, due to the unique funnel-shaped topography of this region and the high population density along the coast (Chutia et al., 2019; Li et al., 2023). For instance, the BoB storm "Nargis (2008)" made landfall at the mouth of the Irrawaddy River in Myanmar on May 2, 2008, with an maximum near surface wind speed of 45.83 m s^{-1} (equivalent to severe typhoon level), which led to over 100,000 deaths or disappearances and was the most devastating storm to hit Myanmar since April 1991 (Li et al., 2023). BoB storms rarely hit China directly; however, they usually cause heavy rainfall and snowstorms over southern Xizang and southwestern Yunnan (Duan and Duan, 2015), often triggering severe secondary disasters such as landslides, mudslides, and flash floods in these mountainous regions. These painful lessons highlight that the accurate forecasts of these storms are crucial for effective disaster risk management, timely evacuation planning, and reducing loss of life and property. However, in contrast with the TCs over the western North Pacific, there is a severe lack of research in the forecasts of BoB storms, and China has begun related researches until

* Corresponding authors.
E-mail addresses: duanws@lasg.iap.ac.cn (W. Duan), yangruowen@ynu.edu.cn (R. Yang).

https://doi.org/10.1016/j.atmosres.2025.108313
Received 4 January 2025; Received in revised form 19 May 2025; Accepted 22 June 2025
Available online 23 June 2025
0169-8095/

2017 (Li et al., 2023). Baki et al. (2013) demonstrated that the current forecast accuracy of BoB storms is significantly lower than that of TCs over the western North Pacific and North Atlantic, although the latter TCs forecasts are still in the urgent need of improvement. Specifically, the track forecast errors for the North Indian Ocean TCs including BoB storms are consistently larger than those of TCs over the western North Pacific and North Atlantic across all prediction time frames, with approximately 24–47 % at lead-time 24 h, 26–75 % at lead time 48 h, and 25–54 % at lead time 72 h (NHC, 2012; RSMC, 2011). Therefore, there is an urgent need to improve the forecast skill of BoB storms and reduce the disaster impacts.

High forecast levels for high-impact weather events generally depend on high accuracy of initial conditions, which are often achieved through assimilating adequate observations. However, the atmospheric observations over the BoB, as well as its surrounding areas, are rare (Baki et al., 2013; Li et al., 2023). Considering the high costs of observing over an extensively large area, Snyder (1996) proposed a concept of "target observation", which involves strategically placing limited observations in some key sensitive areas to achieve or even surpass the forecast skill improvements resulting from widespread observations across the entire region (Rabier et al., 1996; Snyder, 1996; Emanuel et al., 1997; Bergot, 1999). The observation system research and predictability experiment (THORPEX; 2005–2014), which was proposed by the World Meteorological Organization, promoted extensive researches and field campaigns for improving extreme weather events forecast skill, eventually revealing the important role of target observations in improving TC forecast skill (Shapiro and Thorpe, 2004; Aberson, 2011; Majumdar, 2016). Since 2003, the Chinese Taiwan Meteorological Department has started operational field campaigns of target observation for TCs over the western North Pacific (Wu et al., 2007). However, no related studies on BoB storms have been so far reported.

Sensitive areas play an extremely important role in target observation. Many objective methods, e.g., singular vectors (SVs; Palmer et al., 1998), adjoint sensitivity (Baker and Daley, 2000), ensemble transform (Bishop and Toth, 1999), and ensemble transform Kalman filter (Bishop et al., 2001), etc., have been utilized to identify the sensitive areas. However, these methods rely to varying degrees on linear approximation assumptions, which stand in clear theoretical contrast to the inherently nonlinear dynamic characteristics of the atmosphere-ocean system [see the review of Duan et al., 2023]. While this simplified treatment offers some advantages in computational efficiency, it inevitably neglects effect of certain important nonlinear processes. This can lead to significant deviations from the true sensitive areas (Reynolds and Rosmond, 2003; Yu and Meng, 2016). To avoid the limits of the aforementioned linear methods, Mu et al. (2009) proposed using the conditional nonlinear optimal perturbation (CNOP; Mu et al., 2003) method, which fully considers nonlinear processes, to identify the target observation sensitive areas for TC forecasts. Mu et al. (2009) compared CNOP method with SV method and found that the sensitive areas identified by the CNOP for TC track forecasts generally locate in the vortex structure of the TCs, particularly at the juncture with the subtropical high-pressure zone, which clarifies the important roles that TCs and large-scale weather circulation systems play in the amplification of forecast errors in TC track forecasting, highlighting the sensitive areas determined by the CNOP are more physics-relevant. Qin and Mu (2011) extended this comparison to include CNOP, SV, and ETKF, showing that CNOP achieved the largest reduction in forecast error variance of TC tracks. Chen et al. (2013) further confirmed that assimilating real observation data in the sensitive areas identified by the CNOP makes the TC track forecasts comparable to, sometimes better than, assimilating all available data. Especially, several field experiments for TC forecasts have been conducted in recent years, which have verified the effectiveness of the target observations provided by the CNOP method in improving TC track forecast skill (Qin et al., 2022; Feng et al., 2022; Chan et al., 2023). Given these evidence to the superiority of the CNOP, the present study would directly use the CNOP method to identify the sensitive areas of target observation for BoB storm forecasts.

TCs are often characterized by their rapid developments and fast movements, of which implementing the target observations therefore demands high efficiency. In the previous research and field campaigns for target observations using the CNOP method, the identification of the sensitive areas depends on the numerical model and requires high computation costs and relatively longer calculation times. Hence, relatively more time is usually reserved for sensitive area identification. In this situation, model error effects increase and the identified "sensitive areas" may deviate from the actual sensitive area, then degrading the efficacy of the target observations in improving forecast skill. In recent years, big data-driven artificial intelligence (AI) weather models have rapidly developed, demonstrating higher forecast accuracy and computation efficiency than numerical models (Bi et al., 2023; Chen et al., 2023a, 2023b; Lam et al., 2023; Pathak et al., 2023). For example, the "Pangu-Weather" (referred to as "PW" hereafter) model developed by Bi et al. (2023) finishes global 24-h weather forecasts in 1.4 s, which accelerates to 10,000 times as the calculation speed of traditional numerical model. Moreover, Bi et al. (2023) showed that the evaluation of track forecasts for 88 TCs occurring over global ocean basins in 2018 indicated that the forecast skills of the PW model surpassed those of the European Centre for Medium-Range Weather Forecasts (ECMWF). Therefore, utilizing AI models (such as the PW model) may provide an efficient way to identify the sensitive areas for target observations.

It will be innovative to apply the CNOP method to the PW for BoB storm target observations. In this study, we would investigate the uncertainty of the PW with respect to BoB storm track forecasts from the perspective of target observations. Specifically, we would address three questions: (1) How to integrate the CNOP with the PW model to identify the sensitive areas for target observation associated with BoB storm track forecasts? (2) To what extent do the targeted observations improve the forecast skill for BoB storms?, and (3) what are the hints for the PW of the achieved results? The structure of this study is therefore as follows. Section 2 introduces the AI model and data used, followed by the construction of an optimization system for identifying the sensitive areas of target observation for BoB storm track forecasts in Section 3. Section 4 presents the storm cases studied and the corresponding identified sensitive areas, as well as an evaluation of the effectiveness. Finally, Section 5 provides the conclusions and discussion, especially presenting the hints for the PW of the results.

2. The Pangu-Weather model and data

The PW model employs a three-dimensional deep neural network as its core, which is specifically designed for weather forecasting. The deep neural network extracts 3-dimensional atmospheric state information from the meteorological variables at both various pressure levels and surface, and helps the model capture the complex relationships among atmospheric states more accurately. In the PW models, there are five upper-air variables (horizontal wind, temperature, geopotential, and specific humidity) at thirteen pressure levels (1000, 925, 850, 700, 600, 500, 400, 300, 250, 200, 150, 100, and 50 hPa), and four surface variables (10-m height horizontal wind, 2-m height temperature, and mean sea level pressure) at a global 0.25° latitude-longitude grid. Using this AI model to realize the forecasts greatly differs from using traditional numerical model to forecast by step-by-step integration, it employs a hierarchical temporal aggregation algorithm to avoid iterative errors and demonstrates a higher accuracy in longer periods of forecasts. More details can be referred to Bi et al. (2023).

The PW model utilized ERA5 reanalysis data from 1979 to 2017 and trained four models with forecast time intervals of 1 h, 3 h, 6 h, and 24 h. Bi et al. (2023) showed that the PW possesses higher forecast accuracy than the ECMWF-HRES in the track forecasts of the North Indian Ocean TCs including the BoB storms, where the ECMWF-HRES has been widely recognized as one of the premier global numerical forecasting systems.

Nevertheless, this higher accuracy is only reflected as a slightly lower forecast error of PW [see Extended Data Fig. 5. in Bi et al., 2023], and is still far from satisfying the demand for disaster prevention and reduction. Then can targeted observations further improve the forecast skill of the PW with respect to the BoB storm track?

To address this question, we use the ECMWF ERA5 reanalysis data (Hersbach et al., 2020) to drive the PW model. The relevant data have the same configuration as in the PW model's training data (see the last paragraph), but cover the time period from 2019 to 2023, which differs from the PW's training period from 1979 to 2017. Additionally, according to the IBTrACS dataset (Knapp et al., 2010) and Bi et al. (2023), the storm center positions from ERA5 reanalysis data, recorded every 6 h, are connected to form storm tracks, which are used as a reference to evaluate the effectiveness of assimilating targeted observations in improving storm track forecast skill.

For calculating CNOP, we construct the basis of initial perturbations using ensemble forecast data from the ECMWF. These data are provided by the THORPEX Interactive Grand Global Ensemble (TIGGE) project (Bougeault et al., 2010) with a horizontal resolution of 0.5° and include vertical levels at 1000, 925, 850, 700, 500, 300, 250, and 200 hPa. To maintain consistency with the PW model's resolution requirements, we applied bilinear interpolation to convert this data to 0.25° horizontal resolution.

3. The optimization system for sensitive area of target observation in BoB storm forecasts

In this section, we will construct the optimization system for calculating the CNOP and give the approach to identify the sensitive area of target observation associated with the BoB storm track forecasts.

3.1. The CNOP method

Assume the governing equations for atmospheric motion are given by

$$\begin{cases} \dfrac{\partial X}{\partial t} = F(X) \\ X|_{t=0} = X_0 \end{cases} \tag{1}$$

where F represents a nonlinear operator, X is the state vector, and X_0 denotes its initial state. Suppose M_t is the propagator of Eq. (1), then the initial perturbation x_0 superimposed on X_0 can evolve from initial time t_0 to forecast time t through this propagator. At the forecast time t, the evolution of this initial perturbation can be expressed as in Eq. (2).

$$x_t = M_t(X_0 + x_0) - M_t(X_0) \tag{2}$$

Based on the Eq. (2), the following optimization problem is defined,

$$J(x_0^*) = max_{x_0^T C_1 x_0 \le \beta} J(x_0) \tag{3}$$

$$J(x_0) = [M_t(X_0 + x_0) - M_t(X_0)]^T C_2 [M_t(X_0 + x_0) - M_t(X_0)] \tag{4}$$

where $x_0^T C_1 x_0 \le \beta$ represents the constraint on the initial perturbation, $\beta$is a positive scalar limiting the amplitude of the initial perturbation, the superscript "T" denotes the transpose, and C_1 and C_2 are norms that measure the magnitude of the initial perturbation and its evolution, respectively. By solving the Eq. (3), the CNOP-type initial perturbation can be obtained, which represents the initial perturbation that leads to the maximum forecast error at forecast time t (Mu et al., 2003).

For the targeted observation of BoB storm track forecasts in this study, the cost function J of CNOP is specifically expressed as,

$$J(x_0) = [PM_t(X_0 + x_0) - PM_t(X_0)]^T C_2 [PM_t(X_0 + x_0) - PM_t(X_0)] \tag{5}$$

where X_0 is specified as the initial analysis field of control forecast of the BoB storm track and P is the projection operator. For this cost function, $P = 1$ in the region where the BoB storm occurs at forecast time, and $P = 0$ in other regions, thus restricting the region of interest at forecast time to the occurrence area of the BoB storm. The specific region of each storm is dynamically determined to ensure that the spatial extent of the storm at the forecast time is covered. Additionally, both the initial perturbation norm C_1 and the cost function norm C_2 are taken as the total energy (TE) norm, such that

$$x_0{}^T C_1 x_0 = \frac{1}{D_1}\int_{D_1}\int_p \left[u_0{}'^2 + v_0{}'^2 + \frac{c_p}{T_r}T_0{}'^2\right] dpdD_1 \tag{6}$$

$$J = \frac{1}{D_2}\int_{D_2}\int_p \left[u_t{}'^2 + v_t{}'^2 + \frac{c_p}{T_r}T_t{}'^2\right] dpdD_2 \tag{7}$$

where u_0', v_0', T_0' are the components of x_0, representing perturbations in zonal wind, meridional wind, and temperature, respectively; u_t', v_t', T_t'represent the component of x_t [see Eq. (2)] for a particular forecast period (in the present study, we concern about the 72-h forecast); $c_P = 1005.7Jkg^{-1}K^{-1}$ represents the specific heat capacity at constant pressure; $T_r = 270\ K$is the reference temperature; D_1 is the initial perturbation area, which, in this study, is chosen as the geographical domain (70.0°N-70.0°S, 20.0°E-180.0°E), while D_2 is the occurrence area of the BoB storm; and p is the vertical coordinate, with vertical integration from 1000 hPa to 200 hPa. This vertical domain limitation to levels below 200 hPa is due to data availability constraints, as the ECMWF-provided initial perturbation samples used in this study are accessible only for atmospheric levels below 200 hPa. While upper-tropospheric and lower-stratospheric dynamics contribute to TC evolution, the predominant dynamical and thermodynamical processes governing TC development and track are concentrated in the middle and lower troposphere (Chan, 2005; Roy and Kovordányi, 2012), making this vertical domain sufficient for our investigation. Furthermore, the perturbation constraint β is set to be comparable to the variance of the initial analysis error of the variables considered, specifically $\beta = 0.6J/kg$.

With the above calculated CNOP, one can determine the sensitive area for target observation at the initial time t_0 (i.e. the targeting time for increasing additional observations) for the BoB storm track forecast at the forecast time t (also referred to as the lead time t-t_0, which is hereafter referred to as 72 h in this study). In the following section, we will construct the optimization system for calculating the CNOP for identifying the sensitive area for target observations.

3.2. The optimization system and its solving algorithm

This study employs the 6-h (denoted as PW-6) and 24-h (denoted as PW-24) models of the PW to construct the propagator M_t in Eq. (5) through a hierarchical temporal aggregation algorithm (see Fig. 1d). That is, when a forecast has the duration of 24 h starting from t_0, one can use the PW-6 to forecast the state at $t_0 + 6$ h, then again use the PW-6 but with the output at $t_0 + 6$ h as its input to forecast the state at $t_0 + 12$ h, with the output at $t_0 + 12$ h as the input to forecast the state at $t_0 + 18$ h, and eventually use the PW-24 with the state at t_0 as its input to forecast the final state at $t_0 + 24$ h. In our experiments, this kind of construction for the PW has been confirmed to have better performance for the BoB storm track forecasts, as compared with other kinds of constructions of PW-1, −3, −6, and −24 (for simplicity, we omit the details here).

Based on the propagation operator M_t constructed by the PW, the gradient of the cost function J with respect to the initial perturbation x_0 in Eq. (5) can be calculated. Here we usually transform the maximum optimization of Eq. (3) to a minimum one as $J(x_0^*) = min_{x_0^T C_1 x_0 \le \beta} - J(x_0)$, and utilize the spectral projected gradient 2 (SPG2) algorithm (Birgin et al., 2000) to solve this minimization optimization problem based on the calculated gradients. The traditional numerical models typically use the adjoint method, while none is for the PW model to calculate the

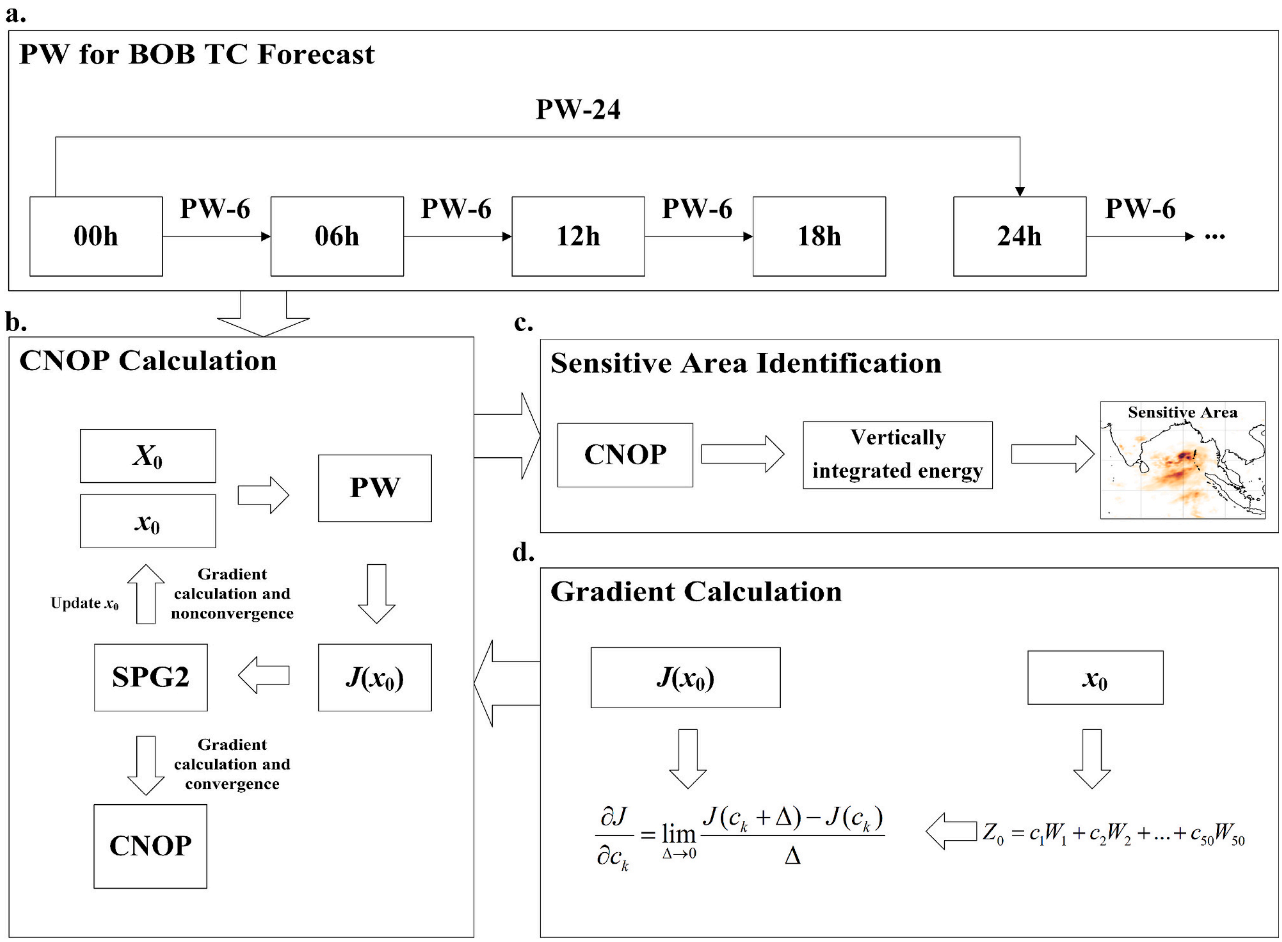

Fig. 1. The construction of the propagator M_t featured by the PW (a), and the flowchart of the optimization system for identifying sensitive areas including CNOP calculation (b) and sensitive area identification (c), and related gradient calculation (d).

gradient. Considering PW's high computation efficiency, this study directly employs the gradient definition to calculate the gradient, then solves the optimization problem, and finally realizes the calculation of CNOP.

For each BoB storm case, we directly use the 50 initial perturbation samples from ECMWF ensemble forecasts [see Section 2] as the basis for constructing the CNOP, due to their excellent orthogonality formed by singular vectors. These basis perturbations are used to construct the initial perturbation Z_0 as a linear combination, as shown in Eq. (8),

$$Z_0 = c_1 W_1 + c_2 W_2 + \ldots + c_{50} W_{50} \quad (8)$$

where W_i represents the initial perturbation sample from ECMWF ensemble forecasts and c_i are constant coefficients to be identified. Replacing x_0 in Eq. (5) with Z_0, the optimal combination of constant coefficients c_i can be obtained by solving the minimum of the objective function of $-J(x_0)$ with respect to the coefficient c_i. That is to say, we transform the optimization problem Eq. (3) from searching for the optimal spatial pattern to solving the optimal combination of constant coefficients c_i, which, undoubtedly, greatly reduces the dimensions of the optimization problem and the computation cost. For this situation, the calculation of the gradient of the cost function J with respect to x_0 is transformed to that of J with respect to c_i, as shown in Eq. (9),

$$\frac{\partial J}{\partial c_k} = \lim_{\Delta \to 0} \frac{J(c_k + \Delta) - J(c_k)}{\Delta}, k = 1, 2, \ldots, 50 \quad (9)$$

Therefore, using the propagator M_t constructed by the PW model, the gradient of the cost function $\frac{\partial J}{\partial c_k}$, and the SPG2 algorithm, the CNOP optimization system for identifying the sensitive areas of target observation associated with the BoB storm forecasts can be constructed. This system comprises four modules (Fig. 1): the PW Model, the CNOP Calculation Module, the Gradient Calculation Module, and the Sensitive Area Identification Module. For each BoB storm case, two forecasts from the PW model using inputs without and with initial perturbations can be obtained, respectively, then the cost function J in Eq. (5), as well as its gradients with respect to the coefficients c_i, can be calculated accordingly. Using these information, the optimal combination of coefficients c_i can be optimized by iterative process using the SPG2 algorithm and the CNOP can be obtained. Then the sensitive area for target observation associated with the BoB storm track forecasts with lead time 72 h can be identified by the approach of comprising the grid points with large values of TE calculated using the CNOP [see Eq. (6)]. This approach has been widely applied in identifying sensitive areas of target observation for western North Pacific TCs (Mu et al., 2009; Zhou and Mu, 2012; Chen et al., 2013; Qin et al., 2022; Feng et al., 2022).

4. CNOP-type initial perturbations and the sensitive areas for BoB storm track forecasts

The sensitive areas for target observations associated with four strong BoB storm track forecasts are identified in this section and the validities are examined by OSSEs. The specific follows.

4.1. The four strong BoB storm cases and their control forecasts

Four strong BoB storm cases are studied. They are the extremely severe cyclonic storm Mocha (2023), the very severe cyclonic storm

Asani (2022), the super cyclonic storm Amphan (2020), and the extremely severe cyclonic storm Bulbul (2019). These four BoB storms brought strong winds, heavy rainfall, and storm surges to the coastal regions of the BoB and led to losses in property and lives. Moreover, the heavy precipitation induced by these BoB storms also affected the Qinghai-Xizang Plateau and southwestern regions of China, which triggered disasters such as mudslides and landslides.

For each BoB storm case, we used respectively the ERA5 data at 12 h, 24 h, and 36 h ahead of the initialized time (i.e. the targeting time for increasing additional observations) of control forecast as its initial conditions, which, due to a small number of storm cases, increases the sample size of control forecasts to make results more robust. For clarity, these three control forecasts are labeled as Ctrl-1, Ctrl-2, and Ctrl-3, all of which provide 72-h forecasts. Table 1 outlines the forecast periods for the four BoB storm cases and the corresponding initial conditions for the control forecasts.

4.2. The CNOP-type initial perturbations and resulted sensitive areas

Using the optimization system detailed in Section 3.2, CNOP-type initial perturbations for 72-h forecasts were computed for the Ctrl-1, −2, and − 3 of each BoB storm case shown in Table 1. Then, a total of twelve CNOP-type initial perturbations were obtained for the four storm cases. As introduced in Section 3.1, the CNOP-type initial perturbations comprise both wind and temperature components. It is shown that, at the lower troposphere (i.e., 850 hPa), the wind components of all CNOP-type initial perturbations are mostly located near the storm centers, exhibiting a cyclonic circulation structure (Fig. 2i, g, and l); however, the temperature component distribution exhibits significant case-dependence: the temperature perturbations for Mocha (2023) and Amphan (2020) show a ring-like distribution centered on the storm (Fig. 2i and k), whereas Bulbul (2019) has large temperature perturbations only on the northeast side of the storm (Fig. 2l), and Asani (2022) has large temperature perturbations near or northwest of the storm center (Fig. 2j).

Results also show that, at the mid-troposphere (500 hPa), the wind components of the CNOP-type initial perturbations are similar in structure to those in the lower troposphere, but the cyclonic nature is somewhat weakened; the temperature perturbations primarily appear on the northeast and southwest sides of the storm center, forming a distinct positive and negative alternating wave train structure; it is additionally noted that, compared to the lower troposphere, the perturbation distribution in the mid-troposphere is more localized either for wind or temperature components (Fig. 2f, g).

In addition, it is demonstrated that, at the upper troposphere (200 hPa), both the wind and temperature components of the CNOP-type initial perturbations show clear case dependence: the Mocha (2023) has positive temperature perturbations on the north or east side of the storm center (Fig. 2a), while the wind perturbations diverge outward from the storm center; the Asani (2022) shows a more dispersed temperature perturbation distribution with significantly reduced perturbation magnitude compared to the mid and lower troposphere, while wind perturbations are mainly distributed near the storm center, forming a cyclonic circulation structure (Fig. 2b); the Bulbul (2019) also has a dispersed temperature perturbation distribution, but the wind field converges inward in Ctrl-1 and -2 and diverges outward from the storm center in Ctrl-3; and the Amphan (2020) has temperature perturbations mainly on the northwest side of the storm and wind perturbations diverging outward from the storm center.

For convenience, all these above CNOP-type perturbations are outlined in Appendices A and B in terms of their spatial characteristics.

For the CNOP-type initial perturbations in Appendices A and B, we also calculated their total perturbation energy (TE) and its components [i.e., kinetic energy (KE) and internal energy (IE)] in the vertical distribution over the BoB region. The results show that, for the Ctrl-1, −2, and − 3 of the same storm case, their CNOP-type initial perturbations exhibit similar characteristics of the vertical distribution of the energies; however, there exists case dependency in the vertical energy distribution of CNOP initial perturbations for different cases. For example, the Mocha (2023), the Asani (2022), and the Amphan (2020) have the CNOP-type perturbations with three energy peaks at 200 hPa, 500 hPa, and 700 hPa, whereas the Bulbul (2019) only has the CNOP-type perturbations with peaks at 200 hPa and 500 hPa; nonetheless, all CNOP-type initial perturbations have the largest total energy in the mid-upper troposphere (500–200 hPa), primarily manifesting as contributions from kinetic energy.

Mu et al. (2009) demonstrated that the grids with large values of CNOP-type initial perturbations represent high sensitivity of forecast uncertainty of high-impact weather events to initial errors. Hence, it is advised to conduct target observation in such areas with priority, which is of great importance to improve the initial condition and further upgrade the forecast skill. Taking the Ctrl-1 for example, Fig. 2 shows both horizontal and vertical energy structures of the CNOP-type initial perturbations for the four BoB storm cases. It is obvious that the areas with large values differ a lot between temperature and wind components and among vertical levels (also see Appendices A and B), which is a great challenge to the implementation of field campaigns. Thus, how can we extract the sensitivity information from the CNOP-type initial perturbations and identify the sensitive areas of target observation that can collectively reflect the sensitivity from varying state variables and their structures? Qin et al. (2013) proposed identifying the sensitive areas of target observation as the grids with large values of the vertically integrated total energy [*VTE*, see Eq. (10)] of the CNOP-type initial perturbations (also see Zhou and Mu, 2011; Chen et al., 2013; Qin et al., 2022; Yang et al., 2022, 2023). Both numerical experiments and related field campaigns have confirmed the effectiveness of the sensitive areas identified using the *VTE* in improving forecast skills (Chan et al., 2023; Feng et al., 2022). Therefore, the *VTE* is also adopted in this study to identify the sensitive areas of target observation for the BoB storm forecasts.

Table 1
BoB storm cases, control forecast initial fields, and forecast periods.

Case	Forecast Period (UTC)	Initial Field for Control Forecast (UTC)	Case	Forecast Period (UTC)	Initial Field for Control Forecast (UTC)	Forecast length
Mocha	1200 May 11, 2023–1200 May 14, 2023	Ctrl-1: Meteorological field at 0000 May 11, 2023 Ctrl-2: Meteorological field at 1200 May 10, 2023 Ctrl-3: Meteorological field at 0000 May 10, 2023	Amphan	1200 May 17, 2020–1200 May 20, 2020	Ctrl-1: Meteorological field at 0000 May 17, 2020 Ctrl-2: Meteorological field at 1200 May 16, 2020 Ctrl-3: Meteorological field at 0000 May 16, 2020	72 h
Asani	0000 May 8, 2022–0000 May 11, 2022	Ctrl-1: Meteorological field at 1200 May 7, 2022 Ctrl-2: Meteorological field at 0000 May 7, 2022 Ctrl-3: Meteorological field at 1200 May 6, 2022	Bulbul	0000 Nov 7, 2019–0000 Nov 10, 2019	Ctrl-1: Meteorological field at 1200 Nov 6, 2019 Ctrl-2: Meteorological field at 0000 Nov 6, 2019 Ctrl-3: Meteorological field at 1200 Nov 5, 2019	72 h

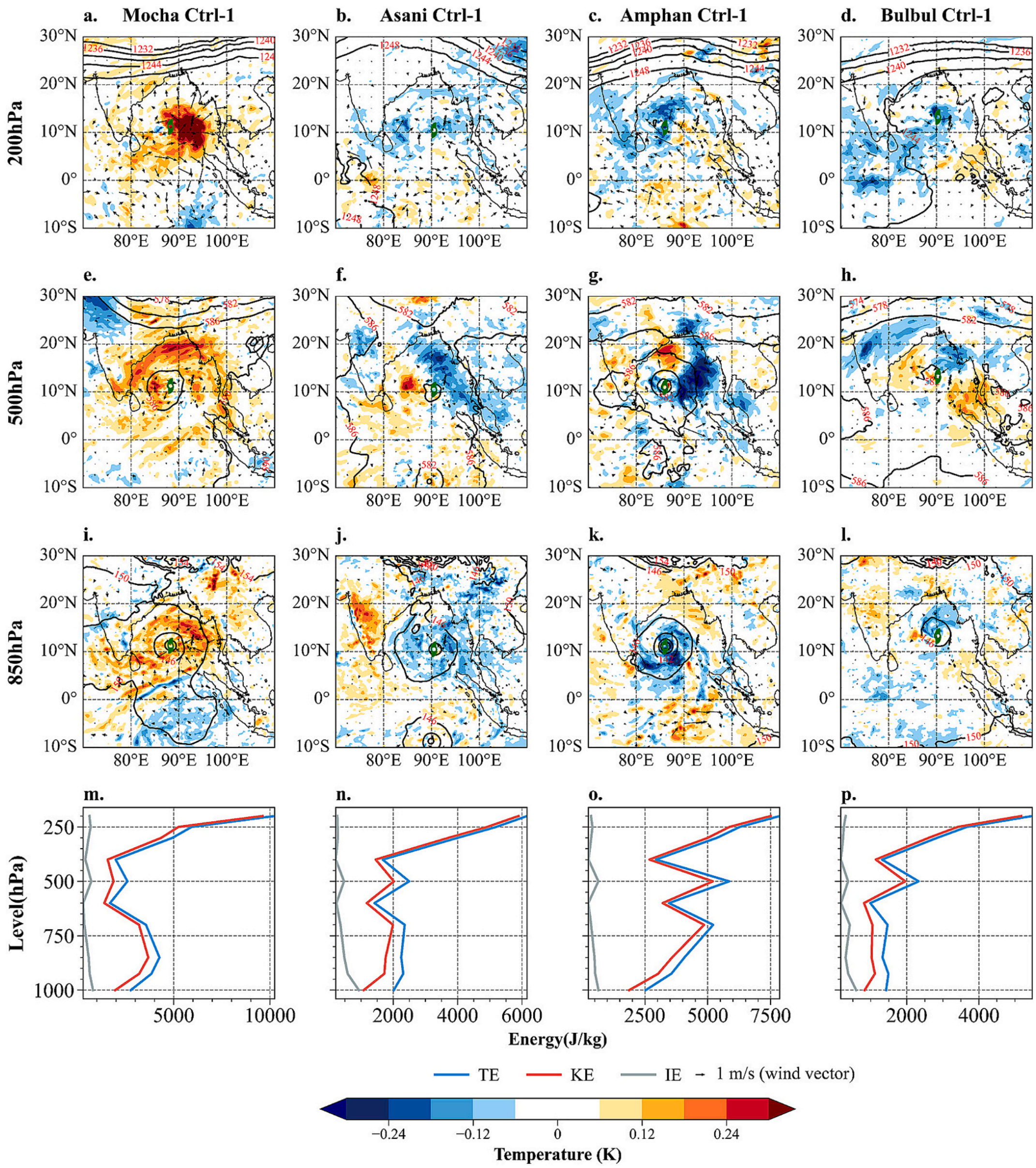

Fig. 2. The wind (vectors; units: m s^{-1}) and temperature (shaded; units: K) components of the CNOP-type initial perturbations at 200 hPa (1st row), 500 hPa (2nd row), and 850 hPa (3rd row) of the Ctrl-1 for the four BoB storms, and the TE (blue line), KE (red line) and IE (gray line) (4th row; units: J/kg). The black contour lines represent the geopotential height (unit: dagpm), and the green storm symbols in the first three rows denote the BoB storm centers at initial time. Note that the CNOP-type initial perturbations for Ctrl-2 and Ctrl-3 of the four BoB storms are plotted in Appendix C. (For interpretation of the references to colour in this figure legend, the reader is referred to the web version of this article.)

$$VTE = \int_p \left[{u_0}'^2 + {v_0}'^2 + \frac{c_p}{T_r} {T_0}'^2 \right] dp \tag{10}$$

Fig. 3 presents the *VTE* of the CNOP-type initial perturbations for the control forecasts of the four BoB storms. Apart from those grids with a long distance from the BoB storm, there is a unanimous area with large *VTE* around the BoB storm centers, which extends to the border of the subtropical high as in the BoB storm cases of the Mocha (2023) and the Amphan (2020). Previous research has established that tropical cyclone track prediction is influenced by two primary categories of factors: environmental field and the cyclone's internal structure (Chan, 2005; Wu and Wang, 2000). The environmental field, particularly the subtropical high-pressure system, plays a dominant role in determining tropical cyclone movement, with cyclones typically moving along the periphery of the subtropical high (Chan and Gray, 1982). The boundary between the cyclone and subtropical high represents a critical region characterized by significant pressure gradients and complex wind variations. This relatively unstable zone is highly sensitive - even small perturbations can substantially alter the environmental steering flow, potentially changing the cyclone's track direction. Simultaneously, a cyclone's internal structure, including its size, intensity, and asymmetric features, can modify how it responds to the environmental steering (Fiorino and Elsberry, 1989). This alignment between high-VTE regions and key meteorological features is not coincidental but rather a direct reflection of the physical processes governing tropical cyclone movement. It is obvious that the distribution of the area with large *VTE* values in the CNOP-type initial perturbations is strongly physics-relevant. For this area, we experimentally regarded the top 5 % grids of the large *VTE* values as the sensitive areas of target observation, which are dotted in blue in Fig. 3.

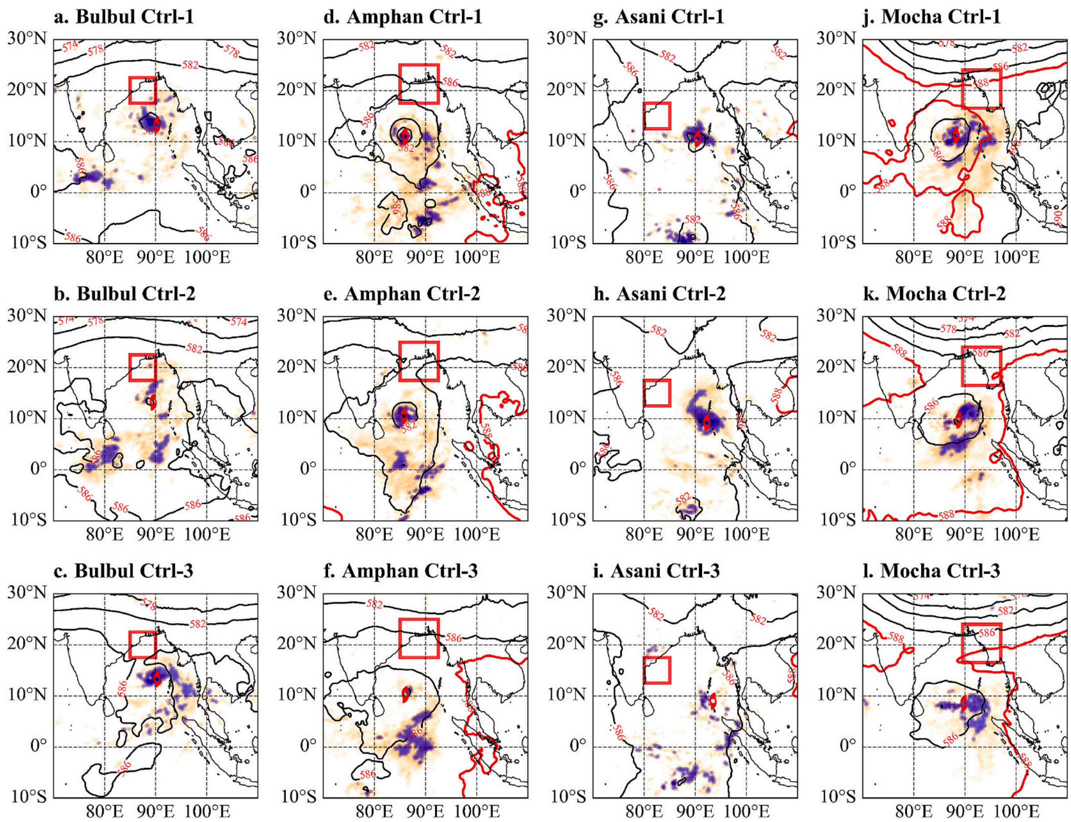

Fig. 3. The *VTE* (shaded) of the CNOP-type initial perturbations of the Ctrl-1, −2, and − 3 for the four BoB storms and corresponding 500 hPa geopotential height (black contour; unit: dagpm). The red storm symbols mark the BoB storm centers at initial time; the red contours denote the 588 dagpm lines, and the blue dots denote the identified sensitive areas of target observations. The red rectangular area represents the D_2 area, i.e. the area where the storm occurs at forecast time. (For interpretation of the references to colour in this figure legend, the reader is referred to the web version of this article.)

4.3. Evaluation of the sensitive areas for target observations

Observing System Simulation Experiments (OSSEs) are utilized in this study to evaluate the impact of the sensitive areas of target observation identified in Section 4.2 on track forecasts. An OSSE involves assimilating simulated observational data into the initial conditions of control forecasts and makes the updated forecasts closer to the truth (which is the state represented by the ECMWF ERA5 reanalysis data in this study). Hence, the effects of the simulated observational data can be illustrated by comparisons between the control forecasts and the updated forecasts. For example, if the simulated observational data inside the sensitive areas is only assimilated, the differences between the control and updated forecasts can directly indicate the effects of additional observations inside the sensitive areas on forecast skill.

Given that the data assimilation system of the PW model is not yet available, we adopted a simple direct update assimilation scheme instead, which directly replaces the initial conditions in some specific areas in the control forecasts with simulated observational data. For each BoB storm case, the initial conditions of the control forecasts in the identified sensitive areas (Fig. 3) were replaced by the ERA5 reanalysis data (i.e. the simulated observational data) at the initial time (i.e., targeting time), which includes horizontal winds and temperature fields from 1000 hPa up to 200 hPa; and the forecasts of PW model based on these initial conditions are denoted as "SEN". Other forecasts were also conducted but with initial conditions of control forecasts that were replaced by those in other thirty randomly selected rectangular areas, which possess the same number of simulated observations as the sensitive area. These forecasts are denoted as "RAN". For convenience, we summarize the key experimental setting in Appendix D.

To evaluate the impact of targeted observations on the forecast skill for BoB storms, this study employed an improved TC tracking algorithm. This algorithm is based on the core logic of the ECMWF tropical cyclone tracker (Magnusson et al., 2021) and has been optimized for the characteristics of the PW model. The algorithm searches for the minimum mean sea level pressure (MSLP) within a 445 km radius around the initial tropical cyclone position, then verifies the TC by checking features including 850 hPa relative vorticity ($>5 \times 10^{-5}$ and local maximum within 278 km radius), 850-200 hPa thickness (local maximum exists), and 10 m wind speed over land (>8 m s^{-1}). Once the existence of a tropical cyclone is confirmed, the tracking algorithm continues to search for the next position within a 445 km radius. Both the BoB storm centers in SEN and RAN were positioned, of which the track forecast errors are denoted as E_{SEN} and E_{RAN}, respectively. A rate "R", as in Eq. (11), is adopted to measure the impacts of additional data in either sensitive areas or randomly selected areas on the control forecasts, where E_{Ctrl} denotes the track forecast errors in the control forecasts. A "R" greater than 0 indicates an improvement; conversely, a R less than 0 means a deterioration; furthermore, the larger (smaller) of the R positive (negative) value, the more significant of the improvement (deterioration).

$$R = \frac{E_{\mathrm{Ctrl}} - E_{\mathrm{SEN\ or\ RAN}}}{E_{\mathrm{Ctrl}}} \times 100\% \tag{11}$$

Fig. 4 shows the moving tracks of the 12 control forecasts for the four storm cases in Table 1, along with those of the corresponding SEN and RAN, as well as the actual track (formed by connecting the storm positions every six hours in the ERA5 reanalysis data). From Fig. 4, it seems that the storm tracks in the SEN are often more deviated from the actual tracks than those in control forecasts and RAN; but actually, the storm tracks in control forecasts and RAN move much slower and have much larger forecast error than those in the SEN especially at the initial stages of forecasts. To quantify the improvement more accurately, the time-

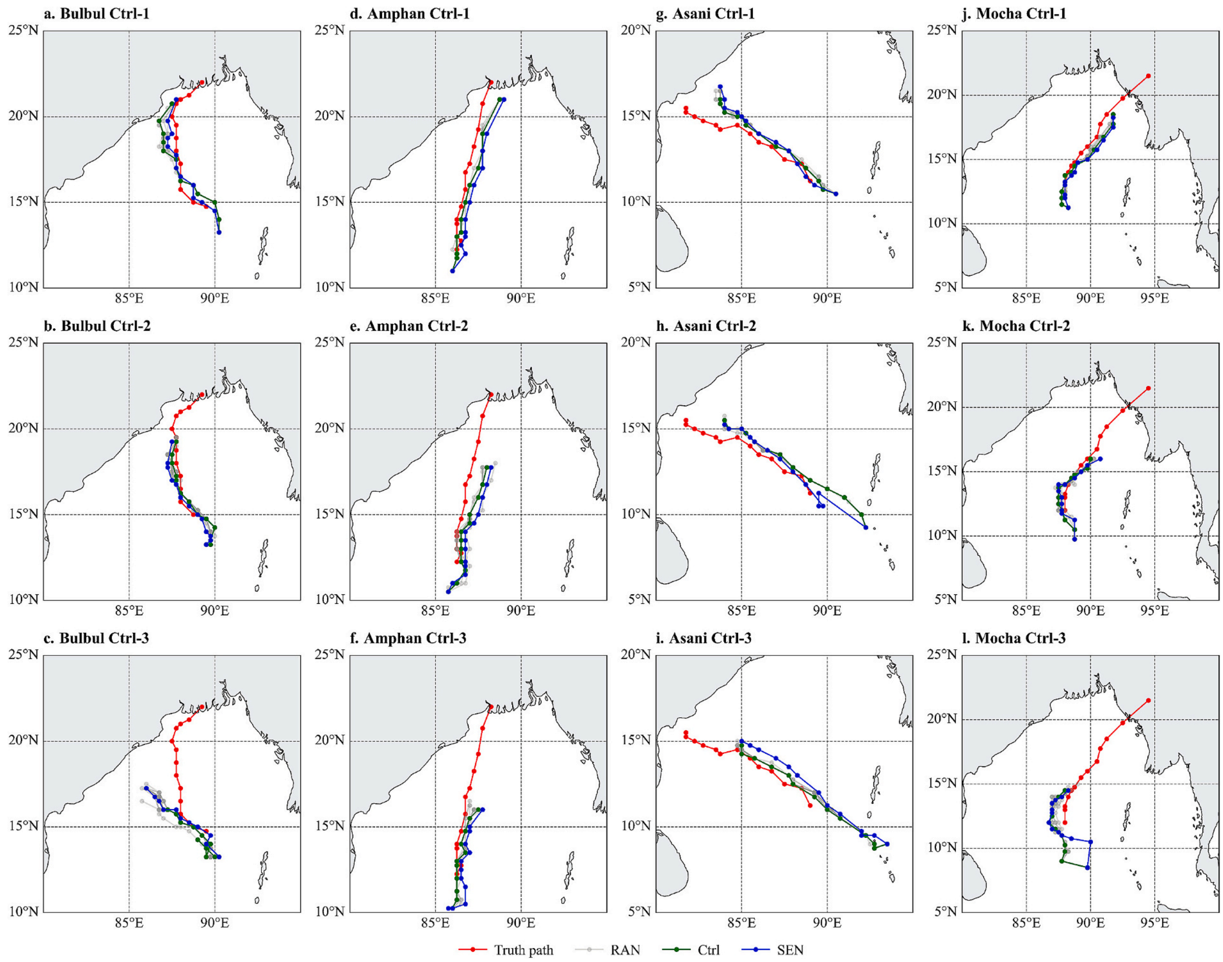

Fig. 4. The forecasts of the BoB storm path in the Ctrl (green), the SEN (blue) and the RAN (gray). The red line represents the truth path. (For interpretation of the references to colour in this figure legend, the reader is referred to the web version of this article.)

dependent "R" was calculated and plotted in Fig. 5a. The results show that, for the forecast duration of less than 24 h, the forecast errors in the SEN are significantly reduced from the control forecasts at the 95 % confidence level, with an averaged skill improvement of 16.54 %; however, as the forecast duration exceeds 24 h, the reduction in forecast errors in the SEN gradually diminishes, and for the forecast duration exceeding 42 h, the forecast errors in the SEN even surpass those of the control forecasts, providing worse forecasts. Thus, although the most sensitive initial perturbations CNOP were calculated for 72-h forecasts for each storm case, the improvement in forecast skill provided by the target observation sensitive areas is only effective within a 24-h forecast duration.

To validate the sensitivity of the target observation sensitive areas, 30 groups of RAN experiments were conducted for each control forecast of each storm case. In these experiments, 30 rectangular regions containing the same number of grid points as in the sensitive area were randomly selected outside the sensitive area of the control forecast to investigate the impact of assimilating enhanced observations on the storm track forecast. To quantify the distance between the sensitive area and each randomly selected region, we identified the grid point with the maximum VTE value within the sensitive area (i.e., the most sensitive point), calculated the distance from this point to the four vertices of each randomly selected rectangular region, and used the shortest distance as the measure between the two regions. We found that the closer the random areas in the RANs are to the sensitive area, the larger the skill improvement of the updated forecast against the control forecast (Fig. 6). However, even so, the skill improvements in the control forecasts in the RANs, even within the 24-h forecast duration, are generally small and far fewer than the improvement in the SENs (Fig. 5b). It is worth noting that for the Ctrl-3 of the storm case Bulbul (2019), although the skill improvement in the RAN is significantly higher than those for other storm cases, it still shows that the closer the randomly selected area is to the sensitive area, the larger the skill improvement in the updated forecasts against the control forecasts, but it remains far below the skill improvement in its SENs (Fig. 6). Therefore, although the skill improvement in storm track forecast skill provided by the sensitive areas is only effective within a 24-h forecast duration, the target observations obtained within these areas represent additional observations with the greatest potential to improve PW's storm track forecasts.

These results imply that using PW to forecast the aforementioned four BoB storm events, the forecast results are sensitive to initial values within a 24-h forecast duration, suggesting that further consideration of PW model errors is needed to enhance PW's forecast skill of BoB storm events for forecasts exceeding a 24-h duration.

4.4. *Mechanism*

As demonstrated in Section 4.2, the CNOP-based sensitive areas mainly locate around the storm center and the boundary to the subtropical high that provides a steering flow of TC movement. Numerous studies have shown that the movements of TCs are primarily dominated by this large-scale steering flow (Chan and Gray, 1982; Holland, 1983; Chan, 2005). Building on this understanding, this section analyzes how

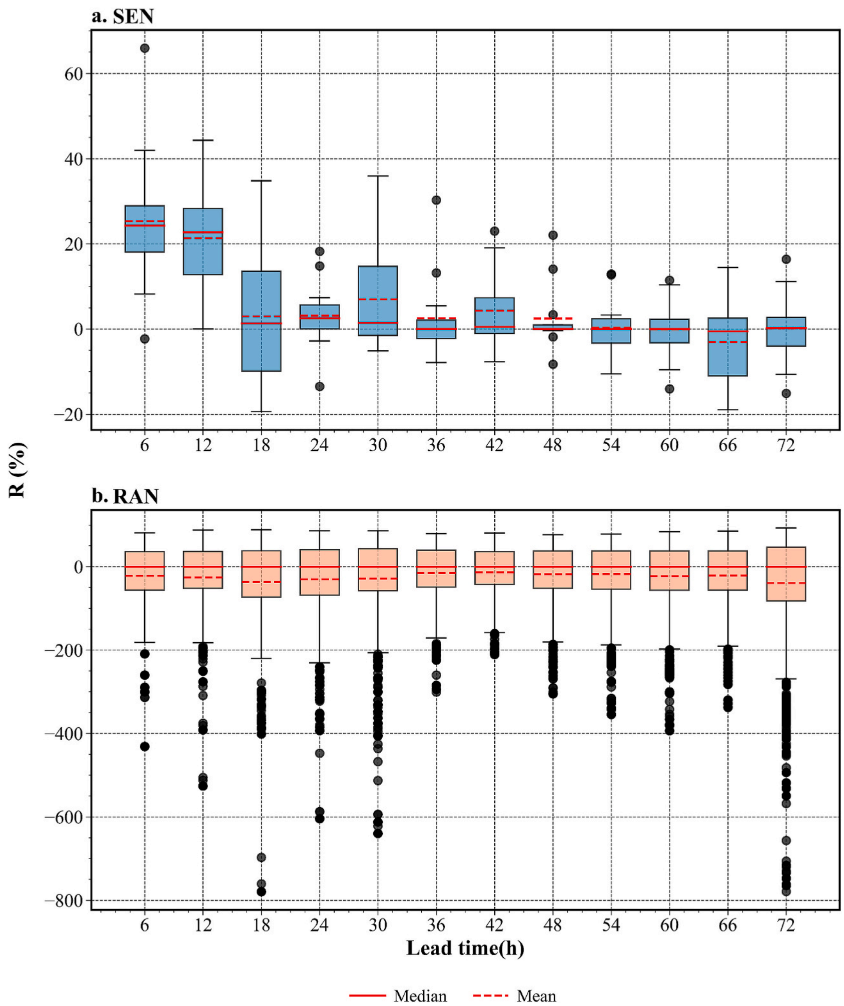

Fig. 5. Box plots of the relative error rate R (%) in (a) SENs and (b) RANs for all control forecasts of the four BoB storms at different lead times (6–72 h). In each box plot, the blue/red box represents the interquartile range (25th to 75th percentiles), the red solid line indicates the median value, the red dashed line shows the mean value, the whiskers extend to 1.5 times the interquartile range, and the black dots represent outliers. Note that different vertical scales are used in panels (a) and (b). (For interpretation of the references to colour in this figure legend, the reader is referred to the web version of this article.)

assimilating additional observations in these sensitive areas improves the representation of steering flows, and consequently enhances track forecast accuracy. Taking the Ctrl-1 experiment of the BoB storm case Bulbul (2019) as an example, we illustrate in Fig. 7 its tracks in the truth, control forecast and the updated forecast due to the target observations. Visibly, the truth path initially moves northwest, then turns north at around 18°N, and finally shifts northeast at 20°N, while the path in the control forecast initially veers east-southeast in the early forecast stage and then is significantly biased westward later on, failing to accurately capture the storm's actual movement path; in contrast, the path in the SEN significantly reduces the deviations observed in the control forecast. To analyze the meteorological mechanisms responsible for the improvement in the SEN, we examined the changes in the steering flow. The steering flow here is defined as the environmental average wind vector within a radius of 4–8° latitude from the storm center. Fig. 8a shows the temporal changes of the steering flow at different vertical heights for the Ctrl-1 and the corresponding SEN, as well as the differences between them. It is shown that the steering flows in both control and SEN initially point northwest and then northeast, consistent with the truth path changes; however, in the early forecast period (i.e., 12-18 h), the steering flow in the SEN contains more southeast wind components in the upper troposphere (250–200 hPa) compared to the control forecast, effectively adjusting the storm path westward. In the mid- to late forecast period (30-54 h), the SEN has more westerly components at 400–200 hPa, leading to a more eastward storm path later on, thus significantly reducing the early eastward and later westward path deviations in the control forecast (see Fig. 7).

Previous research has also indicated that the convergence and divergence of horizontal winds in the upper troposphere significantly affect the development and movement of tropical cyclones. Enhanced divergence of upper-level horizontal winds promotes upward motion and the development of low-level low pressure, thereby steering tropical cyclones toward regions of convergent upward motion (Meng et al., 2002; Liu et al., 2021). Fig. 8b presents the three-dimensional structure of the horizontal wind divergence differences between the Ctrl-1 and SEN of the Bulbul (2019) storm. As shown in Fig. 7b, assimilating sensitive area observations results in a significant increase in divergence on the northwest side of the storm center in the upper troposphere (300–200 hPa), enhancing upward motion and steering the storm toward the northwestern region of upper-level divergence, thus aligning it more closely with the actual path (Fig. 7). These results indicate that assimilating sensitive area observations improved the steering flow in the mid-upper troposphere and the horizontal wind divergence field in the upper troposphere, promoting the storm's northwestward movement and thereby enhancing track forecast skill.

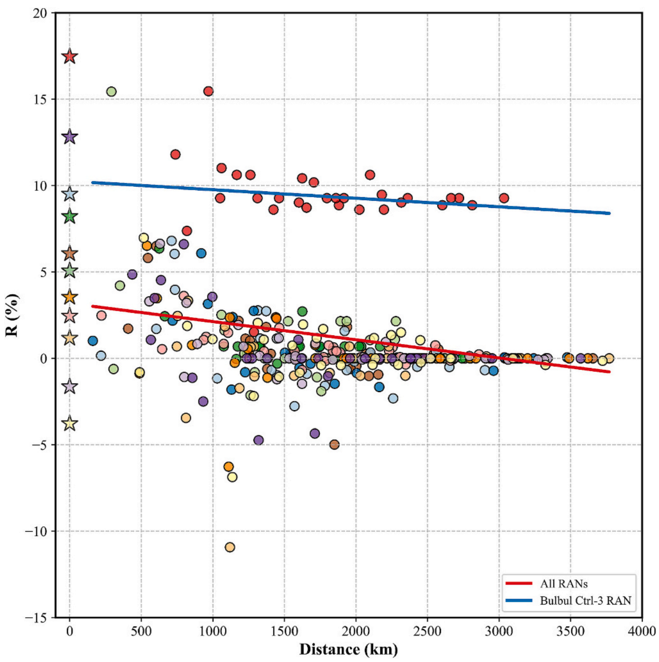

Fig. 6. Scatter plot of the rate R in RANs (colored dots) with respect to the distance between the randomly selected area and sensitive area. The asterisks denote the R in SENs; the red (blue) solid line represents the linear fit for all RANs (RANs for Bulbul (2019) in Ctrl-3). (For interpretation of the references to colour in this figure legend, the reader is referred to the web version of this article.)

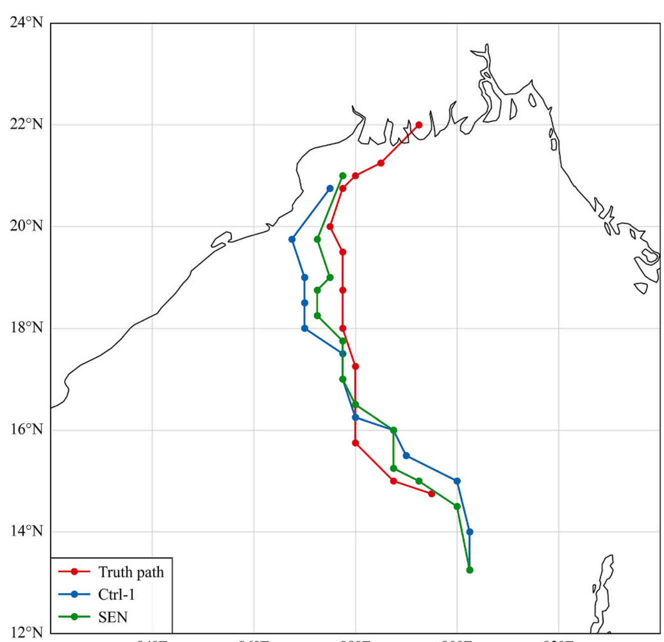

Fig. 7. The forecasts of the BoB storm path in the Ctrl-1 (blue) and the SEN (green) for the BoB storm Bulbul (2019). The red line represents the truth path. (For interpretation of the references to colour in this figure legend, the reader is referred to the web version of this article.)

5. Summary and discussion

Considering linear limitation of traditional methods such as SVs, adjoint sensitivity, and ETKF, etc., quite a few studies adopted the fully nonlinear CNOP method to numerical weather forecast models for identifying the sensitive area for target observations associated with the forecasts of TCs over Northwest Pacific. In the present study, our work extends the CNOP method to an AI weather model for exploring target observation of BoB storm forecasts, which utilizes the high-efficiency of AI model forecasts, and concerns about the disaster weather of BoB storm and then its necessity of accurate forecasts. Actually, the integration of CNOP with the AI-driven PW model represents a step toward computationally-efficient target observation sensitive area identification system, potentially offering practical benefits for field experiments of target observation (see Li et al., 2025).

In this study, we applied the CNOP method to the AI-driven PW model, and developed an optimization system to identify the sensitive areas of target observation for the track forecasts of BoB storms. Four storms of Mocha (2023), Asani (2022), Amphan (2020), and Bulbul (2019) and a total of twelve forecasts of them were investigated. The CNOP-type initial perturbations of the twelve forecasts were calculated using the optimization system, and the sensitive areas were determined through identifying the areas with large values of the vertically integrated energy for those CNOPs. The results showed that the target observation sensitive areas for the forecasts of the four BoB storms were primarily concentrated around the storm center and the boundary with the subtropical high, indicating that these sensitive areas are physically related and reflect the significant influence of the storm's structure and environmental field on its movement.

The study validated the effectiveness of the identified target observation sensitive areas in improving storm event forecast skills through an OSSE. The assimilation of observations in the sensitive areas showed a greater improvement in storm track forecast skills compared to assimilating observations in randomly selected areas. Notably, as the randomly selected areas approached the sensitive areas, the improvement in track forecasts increased, further confirming the rationality of the sensitive areas from another perspective. Using the Bulbul (2019) case as an example, the study elucidated the physical mechanism by which assimilating observations in the sensitive areas improved the steering flow and divergence field in the mid-upper troposphere, thereby enhancing the track forecast skill for the BoB storms.

It must be noted that the improvement in storm track forecasts by assimilating observations in the sensitive areas is mainly evident within the forecast duration of 24 h; and therefore, to further enhance the forecast skill, the impact of model errors must be considered. In other words, for the PW model, merely reducing initial errors is insufficient to improve the track forecast skill of BoB storms for longer lead times; the influence of model errors must also be addressed. Besides, our current study did not investigate the storm intensity forecasts. This limitation stems from inherent constraints of the PW model, that is, the ERA5 reanalysis data that is used for training PW model systematically underestimated TC intensity (Bi et al., 2022); moreover, the relevant spatial resolution $0.25^\circ \times 0.25^\circ$ is insufficient to resolve the small-scale processes crucial for TC intensity evolution. Obviously, the TC intensity forecasts using the PW model need to address model error effect. In previous study, Yao et al. (2021) identified regions that require priority reduction of model error impact using the Nonlinear Forcing Singular Vector (NFSV) method, effectively improving typhoon intensity simulation skills (also see Qin et al., 2020); especially, Duan et al. (2022) recently proposed a combined NFSV method and showed its great ability in resolving combined effect of initial and model errors. It is therefore expected that these NFSV methods can be applied to the BoB storm simulations and forecasts provided by the PW to address model error effects and effectively enhance the simulation and forecast level of track and intensity, especially their long-term forecasts.

Authors statement

The revised version of the manuscript is now submitting to the journal of Atmospheric Research, with the title as "Uncertainty of Pangu-Weathe in Bay of Bengal Storm Track Forecasts: Target

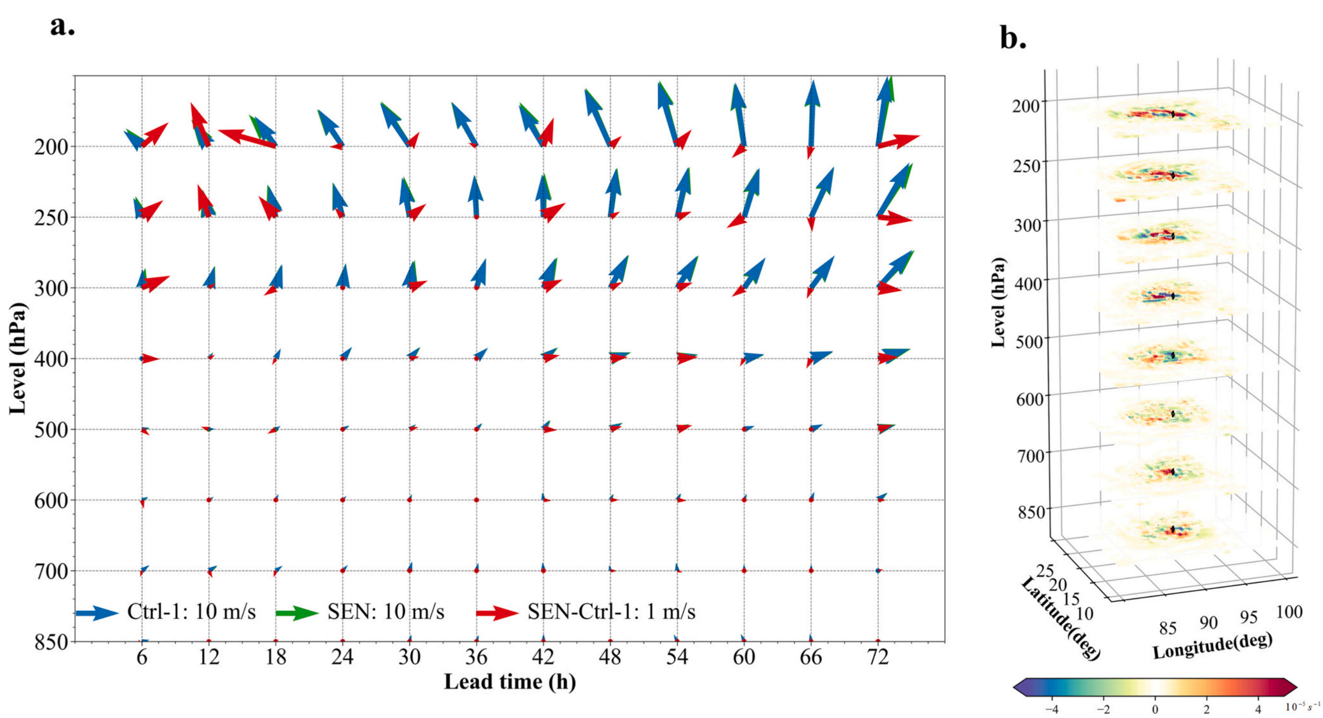

Fig. 8. (a) The steering flows of the forecasts for the Bulbul (2019) Ctrl-1 with blue representing the control forecast, green denoting the SEN, and red signifying the difference between SEN and control; (b) Three-dimensional structure of horizontal wind divergence differences between the control and the SEN for Bulbul (2019) at forecast time 06:00, where the black storm symbol denotes the storm center position. (For interpretation of the references to colour in this figure legend, the reader is referred to the web version of this article.)

Observation Perspective". The article is co-authored by Zeyun Zhou, Wansuo Duan, Ruowen Yang, Xiaohao Qin and Yonghui Li.

We state that the manuscript has been revised according to the comments and suggestions provided by the two reviewers. The content of the manuscript has yet not been published in any journal, and has been solely submitted to the journal of Atmospheric Research. It is expected that the revised manuscript can have positive feedback from editors.

Authors: Wansuo Duan, Zeyun Zhou, Ruowen Yang, Xiaohao Qin, Yonghui Li.

Software availability statement

The Pangu model is available at https://github.com/198808xc/Pangu-Weather.

CRediT authorship contribution statement

Zeyun Zhou: Writing – original draft, Validation, Methodology, Investigation, Formal analysis, Data curation. **Wansuo Duan:** Writing – review & editing, Writing – original draft, Supervision, Methodology, Funding acquisition, Formal analysis, Conceptualization. **Ruowen Yang:** Writing – review & editing, Validation, Supervision, Methodology, Investigation, Formal analysis, Conceptualization. **Xiaohao Qin:** Writing – review & editing, Writing – original draft, Supervision, Investigation, Formal analysis. **Yonghui Li:** Writing – review & editing, Investigation, Data curation.

Declaration of competing interest

The authors declare that they have no known competing financial interests or personal relationships that could have appeared to influence the work reported in this paper.

Acknowledgments

The authors thank the two anonymous reviewers very much for their careful and insightful comments and suggestions. This study was jointly supported by the National Natural Science Foundation of China (Grants 42330111), the Scientific Research and Innovation Project of Postgraduate Students in the Academic Degree of Yunnan University (Grant No. KC-23234374), and the National Key Scientific and Technological Infrastructure project "Earth System Numerical Simulation Facility" (EarthLab).

Appendix A. Distribution characteristics of CNOP initial perturbation wind and temperature components for Mocha (2023) and Asani (2022)

BoB storm Case	Vertical Level	Ctrl-1: CNOP Initial Perturbation		Ctrl-2: CNOP Initial Perturbation		Ctrl-3: CNOP Initial Perturbation	
		Temperature	Wind	Temperature	Wind	Temperature	Wind
Mocha	200 hPa	Positive temperature error north of the storm center	Diverging outward from the storm center	Positive temperature error east of the storm center	Diverging outward from the storm center	Positive temperature error east of the storm center	Diverging outward from the storm center

(*continued on next page*)

(*continued*)

BoB storm Case	Vertical Level	Ctrl-1: CNOP Initial Perturbation		Ctrl-2: CNOP Initial Perturbation		Ctrl-3: CNOP Initial Perturbation	
		Temperature	Wind	Temperature	Wind	Temperature	Wind
	500 hPa	Error on the northwest side of the storm center	Similar to lower levels, but cyclonic intensity is somewhat weakened	Error on the northeast side of the storm center	Similar to lower levels, but wind speed is somewhat reduced	Errors on the northwest and southeast sides of the storm center	Similar to lower levels, but wind speed is somewhat reduced
	850 hPa	Ring-like distribution around the storm center	Cyclonic circulation centered on the storm	Ring-like distribution around the storm center	Converging inward toward the storm center	Ring-like distribution around the storm center	Cyclonic circulation centered on the storm
Asani	200 hPa	More dispersed distribution with significantly reduced errors	Cyclonic circulation centered on the storm with northerly flow on the south side	More dispersed distribution with significantly reduced error magnitude	Cyclonic circulation centered on the storm	More dispersed distribution with significantly reduced error magnitude	Cyclonic circulation centered on the storm with northerly flow on the south side
	500 hPa	Errors on the northeast and west sides of the storm center, forming a positive-negative alternating wave train structure, with pronounced localized error distribution	Similar to lower levels, but wind speed is somewhat reduced	Errors on the northeast and southwest sides of the storm center, forming a positive-negative alternating wave train structure, with pronounced localized error distribution	Similar to lower levels, but cyclonic nature is somewhat weakened	Errors on the northeast and southwest sides of the storm center, with pronounced localized error distribution	Similar to lower levels, but wind speed is somewhat reduced
	850 hPa	Large temperature errors near and northwest of the storm center, more dispersed in other areas	Cyclonic circulation centered on the storm	Large temperature errors near the storm center, more dispersed in other areas	Cyclonic circulation centered on the storm	Large temperature errors near and northwest of the storm center	Westerly flow on the south side of the storm

Appendix B. Distribution characteristics of CNOP initial perturbation wind and temperature components for Amphan (2020) and Bulbul (2019)

BoB storm Case	Vertical Level	Ctrl-1: CNOP Initial Perturbation		Ctrl-2: CNOP Initial Perturbation		Ctrl-3: CNOP Initial Perturbation	
		Temperature	Wind	Temperature	Wind	Temperature	Wind
Amphan	200 hPa	Dispersed distribution	Converging inward toward the storm center	Error on the northwest side of the storm center	Diverging outward from the storm center	Dispersed distribution	Diverging outward from the storm center
	500 hPa	Error on the northeast side of the storm center	Northerly flow on the south side of the storm center	Error on the east side of the storm center	Southerly flow on the south side and westerly flow on the east side of the storm center	Errors on the east and south sides of the storm center	Structure similar to lower levels
	850 hPa	Ring-like distribution around the storm center	Divergent flow field centered on the storm and westerly flow on the south side	Ring-like distribution around the storm center	Cyclonic circulation centered on the storm and easterly flow on the south side	Errors near the storm center and on the south side	Cyclonic circulation centered on the storm and easterly flow on the south side
Bulbul	200 hPa	Dispersed distribution, mainly between 0°-10°N	Converging centered on the storm and easterly flow on the south side	Dispersed distribution	Converging inward toward the storm center	Error on the east side of the storm center	Diverging outward from the storm center
	500 hPa	Errors on the northwest and southeast sides of the storm center, forming a positive-negative alternating wave train structure, with pronounced localized error distribution	Similar to lower levels, but wind speed is somewhat increased	Dispersed distribution	Similar to lower levels, but cyclonic nature is somewhat weakened	Errors on the north and northeast sides of the storm center	Similar to lower levels, but wind speed is somewhat increased
	850 hPa	Error on the north side of the storm center	Cyclonic circulation centered on the storm	Error on the northeast side of the storm center	Cyclonic circulation centered on the storm	Error on the northeast side of the storm center	Cyclonic circulation centered on the storm

Appendix C. CNOP-type initial perturbations (Ctrl-2 and Ctrl-3)

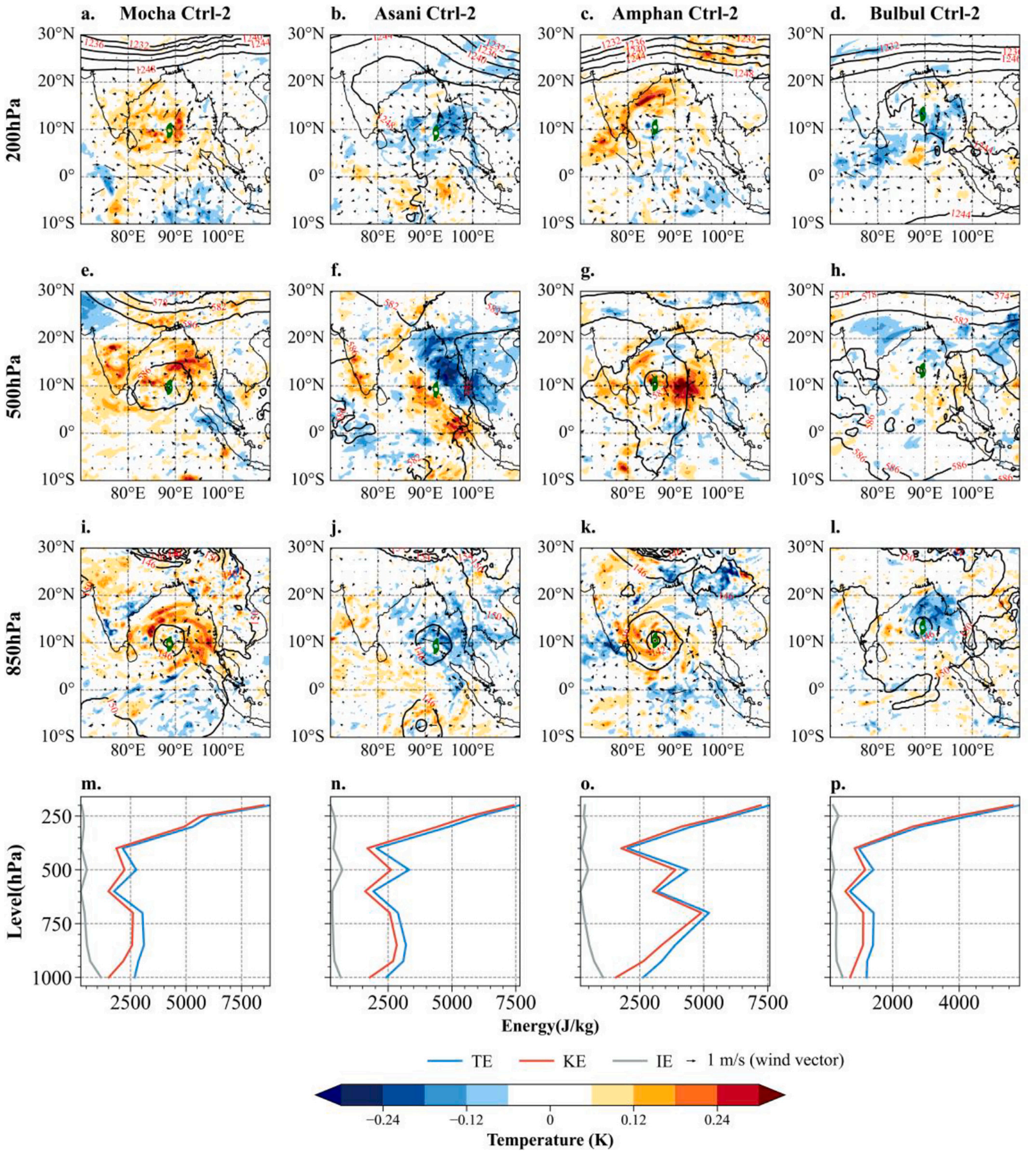

Fig. C1. The wind (vectors; units: m s − 1) and temperature (shaded; units: K) components of the CNOP-type initial perturbations at 200 hPa (1st row), 500 hPa (2nd row), and 850 hPa (3rd row) of the Ctrl-2 for the four BoB storms, and the TE (blue line), KE (red line) and IE (gray line) (4th row; units: J kg − 1). The black contour lines represent the geopotential height (unit: dagpm). The green storm symbols in the first three rows denote the BoB storm centers at initial time. (For interpretation of the references to colour in this figure legend, the reader is referred to the web version of this article.)

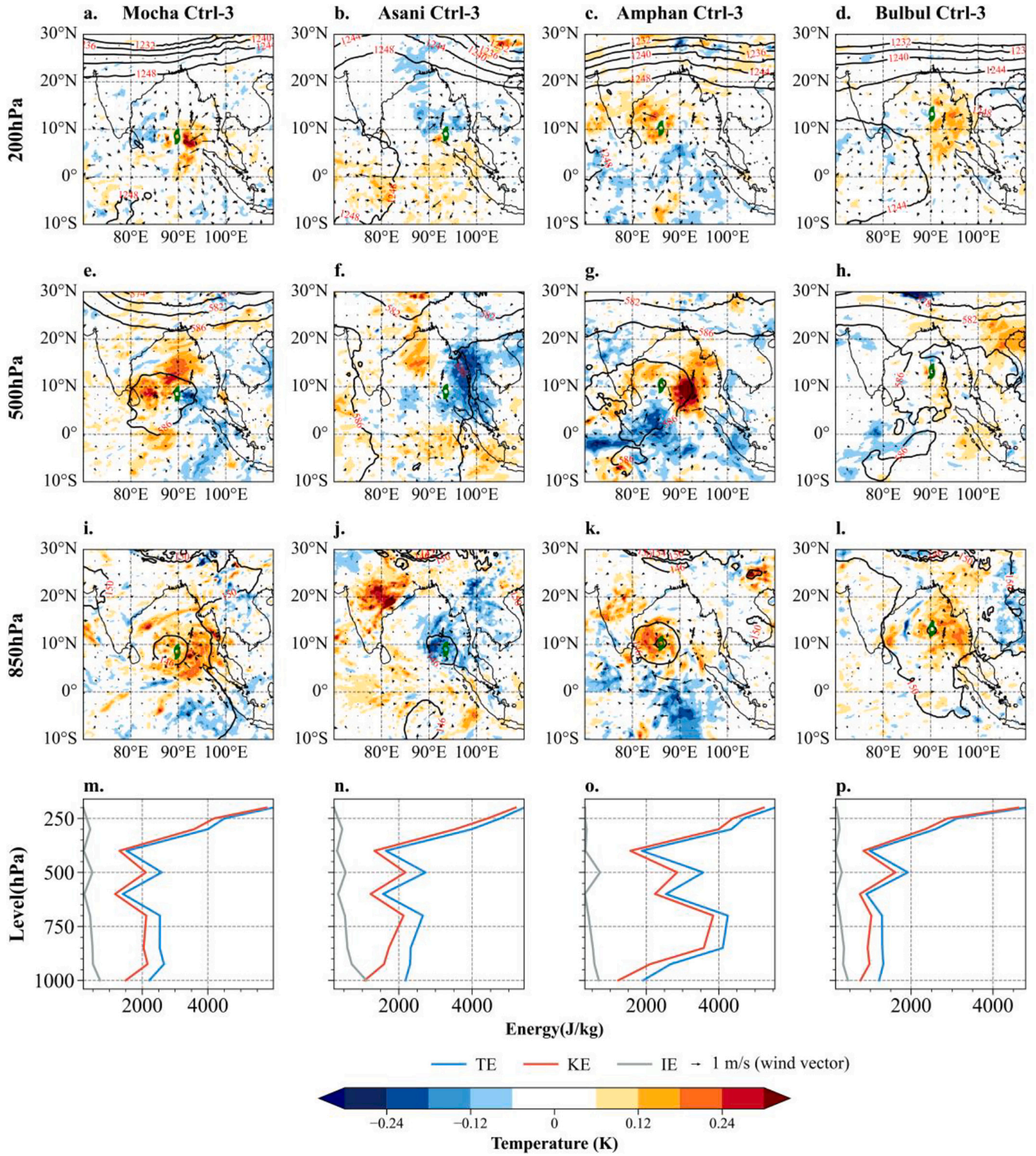

Fig. C2. The wind (vectors; units: m s − 1) and temperature (shaded; units: K) components of the CNOP-type initial perturbations at 200 hPa (1st row), 500 hPa (2nd row), and 850 hPa (3rd row) of the Ctrl-3 for the four BoB storms, and the TE (blue line), KE (red line) and IE (gray line) (4th row; units: J kg − 1). The black contour lines represent the geopotential height (unit: dagpm). The green storm symbols in the first three rows denote the BoB storm centers at initial time. (For interpretation of the references to colour in this figure legend, the reader is referred to the web version of this article.)

Appendix D. Experimental setting

Category	Parameter/Setting	Description/Value
PW Model Configuration	Horizontal Resolution	0.25° × 0.25°
	Vertical Levels	13 pressure levels (1000–50 hPa)
	Forecast Lead Time	72 h
	Output Frequency	6 h
CNOP Method	Optimization Algorithm	SPG2
	Cost Function	Total energy norm at 72 h forecast lead time
	Optimization Domain	(70.0°N-70.0°S, 20.0°E-180.0°E)
	Perturbation Amplitude	0.6 J/kg
	Perturbation Variables	Temperature, u-wind, v-wind (1000–200 hPa)
OSSE Details	"Truth"	ERA5 reanalysis
	Simulated Observations	ERA5 data at initial time (wind, temperature)
	Initial Conditions of Control Forecast	ERA5 at 12, 24, and 36 h ahead of targeting time
	Assimilation Method	Direct update approach
	Sensitive Area Size	Top 5 % *VTE* region (35.0°N-15.0°S, 70.0°E-120°E)
	Random Area Selection	Same number of simulated observations as sensitive area, within domain

Data availability

The ECMWF ERA5 data can be obtained from the Climate Data Store via https://cds.climate.copernicus.eu/.The ECMWF ensemble forecast data is available at https://apps.ecmwf.int/datasets/data/tigge/levtype=pl/type=pf/.

References

Aberson, S.D., 2011. The impact of dropwindsonde data from the THORPEX pacific area regional campaign and the NOAA hurricane field program on tropical cyclone forecasts in the global forecast system. Mon. Weather Rev. 139 (9), 2689–2703. https://doi.org/10.1175/2011MWR3634.1.

Baker, N.L., Daley, R., 2000. Observation and background adjoint sensitivity in the adaptive observation-targeting problem. Q. J. R. Meteorol. Soc. 126 (565), 1431–1454. https://doi.org/10.1002/qj.49712656511.

Baki, H., Chinta, S., Srinivasan, B., Bandyopadhyay, B.K., 2013. Evaluation of official tropical cyclone track forecast over North Indian Ocean issued by India Meteorological Department. J. Earth Syst. Sci. 122 (3), 589–601. https://doi.org/10.1007/s12040-013-0291-1.

Bergot, T., 1999. Adaptive observations during FASTEX: a systematic survey of upstream flights. Q. J. R. Meteorol. Soc. 125 (561), 3271–3298. https://doi.org/10.1002/qj.49712556108.

Bi, K., Xie, L., Zhang, H., Chen, X., Gu, X., Tian, Q., 2022. Pangu-weather: a 3D high-resolution model for fast and accurate global weather forecast. arXiv. https://doi.org/10.48550/arXiv.2211.02556.

Bi, K., Xie, L., Zhang, H., Chen, X., Gu, X., Tian, Q., 2023. Accurate medium-range global weather forecasting with 3D neural networks. Nature 1–6. https://doi.org/10.1038/s41586-023-06185-3.

Birgin, E.G., Martínez, J.M., Raydan, M., 2000. Nonmonotone spectral projected gradient methods on convex sets. SIAM J. Optim. 10 (4), 1196–1211. https://doi.org/10.1137/S1052623497330963.

Bishop, C.H., Toth, Z., 1999. Ensemble Transformation and Adaptive Observations. Retrieved from. https://journals.ametsoc.org/view/journals/atsc/56/11/1520-0469_1999_056_1748_etaao_2.0.co_2.xml.

Bishop, C.H., Etherton, B.J., Majumdar, S.J., 2001. Adaptive Sampling with the Ensemble Transform Kalman Filter. Part I: Theoretical Aspects. Retrieved from. https://journals.ametsoc.org/view/journals/mwre/129/3/1520-0493_2001_129_0420_aswtet_2.0.co_2.xml.

Bougeault, P., Toth, Z., Bishop, C., Brown, B., Burridge, D., Chen, D.H., et al., 2010. The THORPEX interactive grand global ensemble. Bull. Am. Meteorol. Soc. 91 (8), 1059–1072. https://doi.org/10.1175/2010BAMS2853.1.

Chan, J.C.L., 2005. The physics of tropical cyclone motion. Annu. Rev. Fluid Mech. 37 (1), 99–128. https://doi.org/10.1146/annurev.fluid.37.061903.175702.

Chan, J.C.L., Gray, W.M., 1982. Tropical cyclone movement and surrounding flow relationships. Mon. Weather Rev. 110 (10), 1354–1374. https://doi.org/10.1175/1520-0493(1982)110<1354:TCMASF>2.0.CO;2.

Chan, P., Han, W., Mak, B., Qin, X., Liu, Y., Yin, R., Wang, J., 2023. Ground—space—sky observing system experiment during tropical cyclone Mulan in August 2022. Adv. Atmos. Sci. 40, 1–7. https://doi.org/10.1007/s00376-022-2267-z.

Chen, B., Mu, M., Xiaohao, Q., 2013. The impact of assimilating dropwindsonde data deployed at different sites on Typhoon track forecasts. Mon. Weather Rev. 141 (8), 2669–2682. https://doi.org/10.1175/MWR-D-12-00142.1.

Chen, K., Han, T., Gong, J., Bai, L., Ling, F., Luo, J.-J., et al., 2023a. FengWu: pushing the skillful global medium-range weather forecast beyond 10 days Lead. arXiv. https://doi.org/10.48550/arXiv.2304.02948.

Chen, L., Zhong, X., Zhang, F., Cheng, Y., Xu, Y., Qi, Y., Li, H., 2023b. FuXi: a cascade machine learning forecasting system for 15-day global weather forecast. Npj Clim. Atmos. Sci. 6 (1), 1–11. https://doi.org/10.1038/s41612-023-00512-1.

Chutia, L., Pathak, B., Parottil, A., Bhuyan, P.K., 2019. Impact of microphysics parameterizations and horizontal resolutions on simulation of "MORA" tropical cyclone over Bay of Bengal using Numerical Weather Prediction Model. Meteorog. Atmos. Phys. 131 (5), 1483–1495. https://doi.org/10.1007/s00703-018-0651-0.

Duan, X., Duan, W., 2015. Impact of Bay of Bengal storms on precipitation over Plateau Area. Plateau Meteorol. 34 (1), 1–10. https://doi.org/10.7522/j. issn.1000-0534.2014.00001 (in Chinese).

Duan, W., Ma, J., Vannitsem, S., 2022. An ensemble forecasting method for dealing with the combined effects of the initial and model errors and a potential deep learning implementation. Mon. Weather Rev. 150 (11), 2959–2976. https://doi.org/10.1175/MWR-D-22-0007.1.

Duan, W., Yang, L., Mu, M., Wang, B., Shen, X., Meng, Z., Ding, R., 2023. Recent advances in China on the predictability of weather and climate. Adv. Atmos. Sci. 40 (8), 1521–1547. https://doi.org/10.1007/s00376-023-2334-0.

Emanuel, K., Kalnay, E., Bishop, C., Elsberry, R., Gelaro, R., Keyser, D., et al., 1997. Observations in aid of weather prediction for North America: report of prospectus development team seven. Bull. Am. Meteorol. Soc. 78 (12), 2859–2868. https://doi.org/10.1175/1520-0477-78.12.2859.

Feng, J., Qin, X., Wu, C., Zhang, P., Yang, L., Shen, X., et al., 2022. Improving typhoon predictions by assimilating the retrieval of atmospheric temperature profiles from the FengYun-4A's Geostationary Interferometric infrared Sounder (GIIRS). Atmos. Res. 280, 106391. https://doi.org/10.1016/j.atmosres.2022.106391.

Fiorino, M., Elsberry, R.L., 1989. Some aspects of vortex structure related to tropical cyclone motion. J. Atmos. Sci. 46 (7), 975–990. https://doi.org/10.1175/1520-0469(1989)046%3C0975:SAOVSR%3E2.0.CO;2.

Hersbach, H., Bell, B., Berrisford, P., Hirahara, S., Horányi, A., Muñoz-Sabater, J., et al., 2020. The ERA5 global reanalysis. Q. J. R. Meteorol. Soc. 146 (730), 1999–2049. https://doi.org/10.1002/qj.3803.

Holland, G.J., 1983. Tropical cyclone motion: environmental interaction plus a beta effect. J. Atmos. Sci. 40 (2), 328–342. https://doi.org/10.1175/1520-0469(1983)040<0328:TCMEIP>2.0.CO;2.

Knapp, K.R., Kruk, M.C., Levinson, D.H., Diamond, H.J., Neumann, C.J., 2010. The international best track archive for climate stewardship (IBTrACS). Bull. Am. Meteorol. Soc. 91 (3), 363–376. https://doi.org/10.1175/2009BAMS2755.1.

Lam, R., Sanchez-Gonzalez, A., Willson, M., Wirnsberger, P., Fortunato, M., Alet, F., et al., 2023. Learning skillful medium-range global weather forecasting. Science 382 (6677), 1416–1421. https://doi.org/10.1126/science.adi2336.

Li, Y., Qian, C., Fan, X., Liu, B., Ye, W., Lin, J., 2023. Impact of tropical cyclones over the North Indian Ocean on weather in China and related forecasting techniques: a review of progress. J. Meteorol. Res. 37 (2), 192–207. https://doi.org/10.1007/s13351-023-2119-5.

Li, Y., Duan, W., Han, W., Li, H., Qin, X., 2025. Improving tropical cyclone track forecast skill through assimilating target observation achieved by AI-based conditional nonlinear optimal perturbation. J. Geophys. Res. Atmos. 130 (9). https://doi.org/10.1029/2024JD043261 e2024JD043261.

Liang, M., Lin, H., Xu, J., Xu, F., 2020. Statistical analysis on the characteristics of tropical cyclone in the Northern Indian Ocean from 1990 to 2018. J. Guangdong Ocean Univ. 40 (4), 51–59. https://doi.org/10.3969/j.issn.1673-9159.2020.04.008 (in Chinese).

Liu, J., Yan, H., Ye, W., 2021. Effect of atmospheric environmental field on the moving path of storm over the Bay of Bengal in May. J. Meteorol. Sci. 41 (4), 515–525. https://doi.org/10.12306/2019jms.0053 (in Chinese).

Magnusson, L., Majumdar, S., Emerton, R., Richardson, D., Alonso-Balmaseda, M., Baugh, C., et al., 2021. Tropical Cyclone Activities at ECMWF. ECMWF. October. Retrieved from. https://www.ecmwf.int/node/20228.

Majumdar, S.J., 2016. A review of targeted observations. Bull. Am. Meteorol. Soc. 97 (12), 2287–2303. https://doi.org/10.1175/BAMS-D-14-00259.1.

Meng, Z., Chen, L., Xu, X., 2002. Recent progress on tropical cyclone research in China. Adv. Atmos. Sci. 19 (1), 103–110. https://doi.org/10.1007/s00376-002-0037-5.
Mu, M., Duan, W., Wang, B., 2003. Conditional nonlinear optimal perturbation and its applications. Nonlinear Process. Geophys. 10 (6), 493–501. https://doi.org/10.5194/npg-10-493-2003.
Mu, M., Zhou, F., Wang, H., 2009. A method for identifying the sensitive areas in targeted observations for tropical cyclone prediction: conditional nonlinear optimal perturbation. Mon. Weather Rev. 137 (5), 1623–1639. https://doi.org/10.1175/2008MWR2640.1.
NHC USA, 2012. Forecast Verification Report. National Oceanic and Atmospheric Administration. http://www. nhc.noaa.gov/verification.
Palmer, T.N., Gelaro, R., Barkmeijer, J., Buizza, R., 1998. Singular Vectors, Metrics, and Adaptive Observations. Retrieved from. https://journals.ametsoc.org/view/journals/atsc/55/4/1520-0469_1998_055_0633_svmaao_2.0.co_2.xml.
Pathak, J., Subramanian, S., Harrington, P., Raja, S., Chattopadhyay, A., Mardani, M., et al., 2023. FourCastNet: a global data-driven high-resolution weather model using adaptive fourier neural operators. arXiv. https://doi.org/10.48550/arXiv.2202.11214. July 20.
Qin, X., Mu, M., 2011. A study on the reduction of forecast error variance by three adaptive observation approaches for tropical cyclone prediction. Mon. Weather Rev. 139 (7), 2218–2232. https://doi.org/10.1175/2010MWR3327.1.
Qin, X., Duan, W., Mu, M., 2013. Conditions under which CNOP sensitivity is valid for tropical cyclone adaptive observations. Q. J. R. Meteorol. Soc. 139 (675), 1544–1554. https://doi.org/10.1002/qj.2109.
Qin, X., Duan, W., Xu, H., 2020. Sensitivity to tendency perturbations of tropical cyclone short-range intensity forecasts generated by WRF. Adv. Atmos. Sci. 37 (3), 291–306. https://doi.org/10.1007/s00376-019-9187-6.
Qin, X., Duan, W., Chan, P.-W., Chen, B., Huang, K.-N., 2022. Effects of dropsonde data in field campaigns on forecasts of tropical cyclones over the Western North Pacific in 2020 and the role of CNOP sensitivity. Adv. Atmos. Sci. https://doi.org/10.1007/s00376-022-2136-9.
Rabier, F., Klinker, E., Courtier, P., Hollingsworth, A., 1996. Sensitivity of forecast errors to initial conditions. Q. J. R. Meteorol. Soc. 122 (529), 121–150. https://doi.org/10.1256/smsqj.52905.
Reynolds, C.A., Rosmond, T.E., 2003. Nonlinear growth of singular-vector-based perturbations. Q. J. R. Meteorol. Soc. 129 (594), 3059–3078. https://doi.org/10.1256/qj.02.193.
Roy, C., Kovordányi, R., 2012. Tropical cyclone track forecasting techniques — a review. Atmos. Res. 104–105, 40–69. https://doi.org/10.1016/j.atmosres.2011.09.012.
Shapiro, M.A., Thorpe, A.J., 2004. THORPEX International Science Plan.
Snyder, C., 1996. Summary of an informal workshop on adaptive observations and FASTEX. Bull. Am. Meteorol. Soc. 77 (5), 953–961. https://doi.org/10.1175/1520-0477-77.5.953.
RSMC Tokyo, 2011. Annual Report on Activities of the RSMC Tokyo Typhoon Center. https://www.data.jma.go.jp/typhoon/verification.
Wu, L., Wang, B., 2000. A potential vorticity tendency diagnostic approach for tropical cyclone motion*. Mon. Weather Rev. 128 (6), 1899–1911. https://doi.org/10.1175/1520-0493(2000)128%3C1899:APVTDA%3E2.0.CO;2.
Wu, C.-C., Chou, K.-H., Lin, P.-H., Aberson, S.D., Peng, M.S., Nakazawa, T., 2007. The impact of dropwindsonde data on typhoon track forecasts in DOTSTAR. Weather Forecast. 22 (6), 1157–1176. https://doi.org/10.1175/2007WAF2006062.1.
Yang, L., Duan, W., Wang, Z., Yang, W., 2022. Toward targeted observations of the meteorological initial state for improving the PM2.5forecast of a heavy haze event that occurred in the Beijing–Tianjin–Hebei region. Atmos. Chem. Phys. 22 (17), 11429–11453. https://doi.org/10.5194/acp-22-11429-2022.
Yang, L., Duan, W., Wang, Z., 2023. An approach to refining the ground meteorological observation stations for improving PM2.5 forecasts in the Beijing–Tianjin–Hebei region. Geosci. Model Dev. 16 (13), 3827–3848. https://doi.org/10.5194/gmd-16-3827-2023.
Yao, J., Duan, W., Qin, X., 2021. Which features of the SST forcing error most likely disturb the simulated intensity of tropical cyclones? Adv. Atmos. Sci. 38 (4), 581–602. https://doi.org/10.1007/s00376-020-0073-z.
Yu, H., Meng, Z., 2016. Key synoptic-scale features influencing the high-impact heavy rainfall in Beijing, China, on 21 July 2012. Tellus A 68 (1), 31045. https://doi.org/10.3402/tellusa.v68.31045.
Zhou, F., Mu, M., 2011. The impact of verification area design on tropical cyclone targeted observations based on the CNOP method. Adv. Atmos. Sci. 28 (5), 997–1010. https://doi.org/10.1007/s00376-011-0120-x.
Zhou, F., Mu, M., 2012. The time and regime dependencies of sensitive areas for tropical cyclone prediction using the CNOP method. Adv. Atmos. Sci. 29 (4), 705–716. https://doi.org/10.1007/s00376-012-1174-0.